



Universiteit
Leiden
The Netherlands

15NH₃ in the atmosphere of a cool brown dwarf

Barrado, D.; Mollière, P.; Patapis, P.; Min, M.; Tremblin, P.; Ardevol Martinez, F.; ... ;
Wright, G.

Citation

Barrado, D., Mollière, P., Patapis, P., Min, M., Tremblin, P., Ardevol Martinez, F., ... Wright, G. (2023). 15NH₃ in the atmosphere of a cool brown dwarf. *Nature*, 624, 263-266.
doi:10.1038/s41586-023-06813-y

Version: Publisher's Version

License: [Licensed under Article 25fa Copyright Act/Law \(Amendment Taverne\)](#)

Downloaded from: <https://hdl.handle.net/1887/3716589>

Note: To cite this publication please use the final published version (if applicable).

$^{15}\text{NH}_3$ in the atmosphere of a cool brown dwarf

<https://doi.org/10.1038/s41586-023-06813-y>

Received: 11 July 2023

Accepted: 31 October 2023

Published online: 6 November 2023

 Check for updates

David Barrado^{1,26}, Paul Mollière^{2,26}, Polychronis Patapis^{3,26}, Michiel Min⁴, Pascal Tremblin⁵, Francisco Ardevol Martínez^{4,6,7,8}, Niall Whiteford⁹, Malavika Vasist¹⁰, Ioannis Argyriou¹¹, Matthias Samland², Pierre-Olivier Lagage¹², Leen Decin¹¹, Rens Waters^{4,13}, Thomas Henning², María Morales-Calderón¹, Manuel Guedel^{2,3,14}, Bart Vandenbussche¹¹, Olivier Absil¹⁰, Pierre Baudoz¹⁵, Anthony Boccaletti¹⁵, Jeroen Bouwman², Christophe Cossou¹⁶, Alain Coulais^{12,17}, Nicolas Crouzet¹⁸, René Gastaud¹⁶, Alistair Glasse¹⁹, Adrian M. Glauser³, Inga Kamp⁶, Sarah Kendrew²⁰, Oliver Krause², Fred Lahuis⁴, Michael Mueller⁶, Göran Olofsson²¹, John Pye²², Daniel Rouan¹⁵, Pierre Royer¹¹, Silvia Scheithauer², Ingo Waldmann²³, Luis Colina¹, Ewine F. van Dishoeck¹⁸, Tom Ray²⁴, Göran Östlin²⁵ & Gillian Wright¹⁹

Brown dwarfs serve as ideal laboratories for studying the atmospheres of giant exoplanets on wide orbits, as the governing physical and chemical processes within them are nearly identical^{1,2}. Understanding the formation of gas-giant planets is challenging, often involving the endeavour to link atmospheric abundance ratios, such as the carbon-to-oxygen (C/O) ratio, to formation scenarios³. However, the complexity of planet formation requires further tracers, as the unambiguous interpretation of the measured C/O ratio is fraught with complexity⁴. Isotope ratios, such as deuterium to hydrogen and $^{14}\text{N}/^{15}\text{N}$, offer a promising avenue to gain further insight into this formation process, mirroring their use within the Solar System^{5–7}. For exoplanets, only a handful of constraints on $^{12}\text{C}/^{13}\text{C}$ exist, pointing to the accretion of ^{13}C -rich ice from beyond the CO iceline of the disks^{8,9}. Here we report on the mid-infrared detection of the $^{14}\text{NH}_3$ and $^{15}\text{NH}_3$ isotopologues in the atmosphere of a cool brown dwarf with an effective temperature of 380 K in a spectrum taken with the Mid-Infrared Instrument (MIRI) of JWST. As expected, our results reveal a $^{14}\text{N}/^{15}\text{N}$ value consistent with star-like formation by gravitational collapse, demonstrating that this ratio can be accurately constrained. Because young stars and their planets should be more strongly enriched in the ^{15}N isotope¹⁰, we expect that $^{15}\text{NH}_3$ will be detectable in several cold, wide-separation exoplanets.

The coldest class of brown dwarfs, so-called Y dwarfs, span temperatures from 250 to 500 K (ref. 11). Their atmospheres are dominated by the absorption of water, methane and ammonia, whereas water clouds probably become important for the colder Y dwarfs¹². Because their emission peaks in the mid-infrared beyond 4 μm , Y-dwarf spectroscopic characterization is challenging and the number of studies has been limited^{12–14}. The JWST is transforming the study of Y dwarfs by allowing access to their full luminous range¹⁵. We analysed JWST/MIRI Medium Resolution Spectrometer (MRS)¹⁶ observations of the Y-dwarf archetype WISEP J182831.08 + 265037.8 (hereafter WISE J1828),

with an effective temperature of about 380 K (ref. 11). We obtain a mid-infrared spectrum at $R \approx 3,000$ to 1,500, between 4.9 and 27.9 μm . The data reduction is described in Methods. Our observations are presented in Fig. 1, together with an exemplary best-fit model from our analysis, and reveal a spectrum rich in molecular features, namely, a broad water-absorption band at 5–7 μm , methane at 7.6 μm and ammonia at 9–13 μm . The ammonia band is also shown in more detail in the lower panels of Fig. 1. We analysed the atmospheric properties of WISE J1828 using several retrieval codes^{17–19} and self-consistent atmosphere models in radiative-convective equilibrium (refs. 20,21

¹Centro de Astrobiología (CAB), CSIC-INTA, Madrid, Spain. ²Max-Planck-Institut für Astronomie (MPIA), Heidelberg, Germany. ³Institute of Particle Physics and Astrophysics, ETH Zurich, Zürich, Switzerland. ⁴SRON Netherlands Institute for Space Research, Leiden, The Netherlands. ⁵Université Paris-Saclay, UVSQ, CNRS, CEA, Gif-sur-Yvette, France. ⁶Kapteyn Institute of Astronomy, University of Groningen, Groningen, The Netherlands. ⁷School of GeoSciences, University of Edinburgh, Edinburgh, UK. ⁸Centre for Exoplanet Science, University of Edinburgh, Edinburgh, UK. ⁹Department of Astrophysics, American Museum of Natural History, New York, NY, USA. ¹⁰STAR Institute, Université de Liège, Liège, Belgium. ¹¹Institute of Astronomy, KU Leuven, Leuven, Belgium. ¹²Université Paris-Saclay, Université Paris Cité, CEA, CNRS, AIM, Gif-sur-Yvette, France. ¹³Department of Astrophysics/IMAPP, Radboud University, Nijmegen, The Netherlands. ¹⁴Department of Astrophysics, University of Vienna, Vienna, Austria. ¹⁵LESIA, Observatoire de Paris, Université PSL, CNRS, Sorbonne Université, Université de Paris Cité, Meudon, France. ¹⁶Université Paris-Saclay, CEA, IRFU, Gif-sur-Yvette, France. ¹⁷LERMA, Observatoire de Paris, Université PSL, CNRS, Sorbonne Université, Paris, France. ¹⁸Leiden Observatory, Leiden University, Leiden, The Netherlands. ¹⁹UK Astronomy Technology Centre, Royal Observatory Edinburgh, Edinburgh, UK. ²⁰European Space Agency, Space Telescope Science Institute, Baltimore, MD, USA. ²¹Department of Astronomy, Stockholm University, AlbaNova University Center, Stockholm, Sweden. ²²School of Physics & Astronomy, Space Research Centre, Space Park Leicester, University of Leicester, Leicester, UK. ²³Department of Physics and Astronomy, University College London, London, UK. ²⁴School of Cosmic Physics, Dublin Institute for Advanced Studies, Dublin, Ireland. ²⁵Department of Astronomy, Oskar Klein Centre, Stockholm University, Stockholm, Sweden. ²⁶These authors contributed equally: David Barrado, Paul Mollière, Polychronis Patapis. ✉e-mail: barrado@cab.inta-csic.es

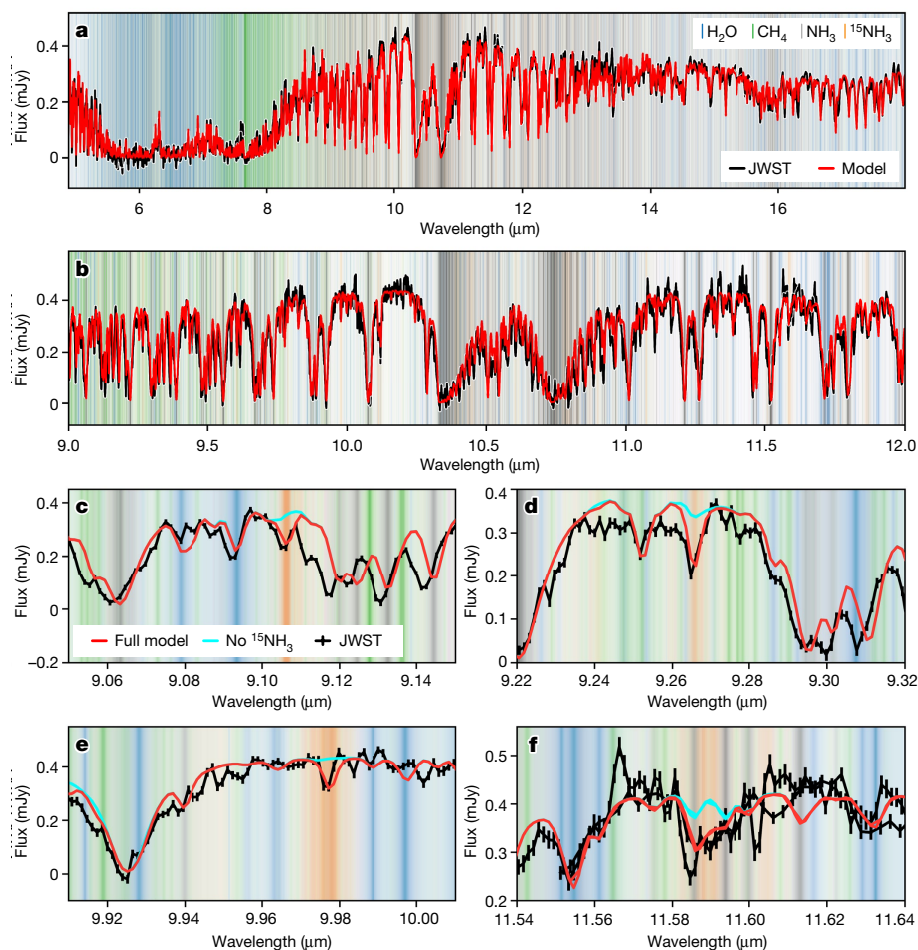


Fig. 1 | MIRI/MRS spectrum and exemplary best-fit model (here, pRT-free) of the Y dwarf WISE J1828. a, Full MIRI wavelength range considered in our models at retrieval resolution ($\lambda/\Delta\lambda = 1,000$). All other panels show the data at the original, higher MRS resolution; models have been post-processed to the same resolution. **b**, As in **a** but zoomed in to show the NH_3 absorption band at

10 μm in more detail. **c–f**, Individual $^{15}\text{NH}_3$ lines in the data, including a best-fit retrieval model with and without accounting for the opacity of $^{15}\text{NH}_3$. The error bars shown for the observations correspond to 1σ confidence levels. Panel **f** contains two overlapping MIRI/MRS subchannels. Coloured bands denote the theoretical positions of the absorption lines of H_2O , CH_4 , NH_3 and $^{15}\text{NH}_3$.

and F.A.M. et al., manuscript in preparation). The best-fit spectra and residuals are shown in Extended Data Fig. 1. As the MIRI observations mostly explore high altitudes in the atmosphere (with the contribution function peaking at approximately 1 bar), we also added archival near-infrared data¹⁴, which examines deeper layers, at pressures of about 10 bar (Extended Data Fig. 2). Owing to its high luminosity, given its spectral type, WISE J1828 is suggested to be a binary system (However, numerous studies, including recent JWST measurements, all failed at resolving its binarity, putting an upper limit of 0.5 AU on the separation of its components^{11,22}). We thus modelled WISE J1828 as an equal-mass binary system, emitting with identical atmospheres.

By combining the results of different retrieval approaches (see Methods), we constrain the \log_{10} (volume mixing ratios) (VMRs) of the conspicuous absorbers H_2O , CH_4 and $^{14}\text{NH}_3$ to be $-3.03^{+0.18}_{-0.21}$, $-3.65^{+0.21}_{-0.21}$ and $-4.79^{+0.15}_{-0.25}$, respectively. The surface gravity of WISE J1828 is constrained to be $\log(g) = 4.34^{+0.42}_{-0.88}$, the effective temperature is 378^{+13}_{-18} K and the radius is constrained to $1.37^{+0.26}_{-0.13} R_{\text{Jup}}$. The uncertainties for these values are dominated by the dispersion between the various fitting approaches and are thus larger than the actual uncertainties derived from any single analysis. A posterior plot of the various retrievals is shown in the Extended Data Fig. 3, whereas all retrieval results are summarized in Extended Data Table 1. The self-consistent models constrain the atmospheric properties to be $\log(g) = 4.5 \pm 1.0$, $R = 1.27 \pm 0.21 R_{\text{Jup}}$ and $T_{\text{eff}} = 450 \pm 101$ K. Again, the reported uncertainties are dominated by differences between the two models. Our best-fit values

of $\log(g)$, R and T_{eff} , after applying a binary correction to the inferred radii (dividing by $\sqrt{2}$), indicate an age of roughly 5 Gyr for an approximately $15-M_{\text{Jup}}$ equal-mass binary system²³, which is consistent with our mass constraints (see Extended Data Table 2).

The metallicity we derive for WISE J1828, combining the results of all approaches that included it as a free parameter (retrievals and self-consistent), is consistent with solar: $[\text{M}/\text{H}] = 0.02^{+0.12}_{-0.31}$. For C/O, we find $0.22^{+0.37}_{-0.03}$ (solar is 0.55 ± 0.10 (ref. 24)), whereas N/O is constrained to $0.014^{+0.021}_{-0.002}$ (solar is 0.138 ± 0.023 (ref. 24)). These uncertainties are again dominated by the dispersion between different approaches. The resulting posteriors for the metallicity, C/O and N/O are shown in Extended Data Fig. 3. Our findings thus indicate an atmosphere with a solar bulk metallicity, but depleted in C and N. A probable cause for this is a departure from chemical equilibrium, in which gas poor in both NH_3 and CH_4 is mixed up from the deep interior of the object²⁵. The resulting gas would be enriched in N_2 and CO, to which our observations are not sensitive. N_2 is not spectrally active, and our shortest wavelengths are longer than the location of the fundamental band of CO at roughly $4.5 \mu\text{m}$. However, it is questionable whether enough CO can be mixed up from the deep atmosphere to palpably change the inferred C/O ratio²⁶.

Also, we detect $^{15}\text{NH}_3$ with a significance ranging from 4σ to 6σ , with several lines of ammonia clearly visible in the data (see Fig. 1). We derive a VMR of $-7.68^{+0.24}_{-0.34}$ for $^{15}\text{NH}_3$ and $^{14}\text{N}/^{15}\text{N} = 670^{+390}_{-211}$, averaging over the results of various models. In Fig. 2, we summarize $^{14}\text{N}/^{15}\text{N}$ for a range of

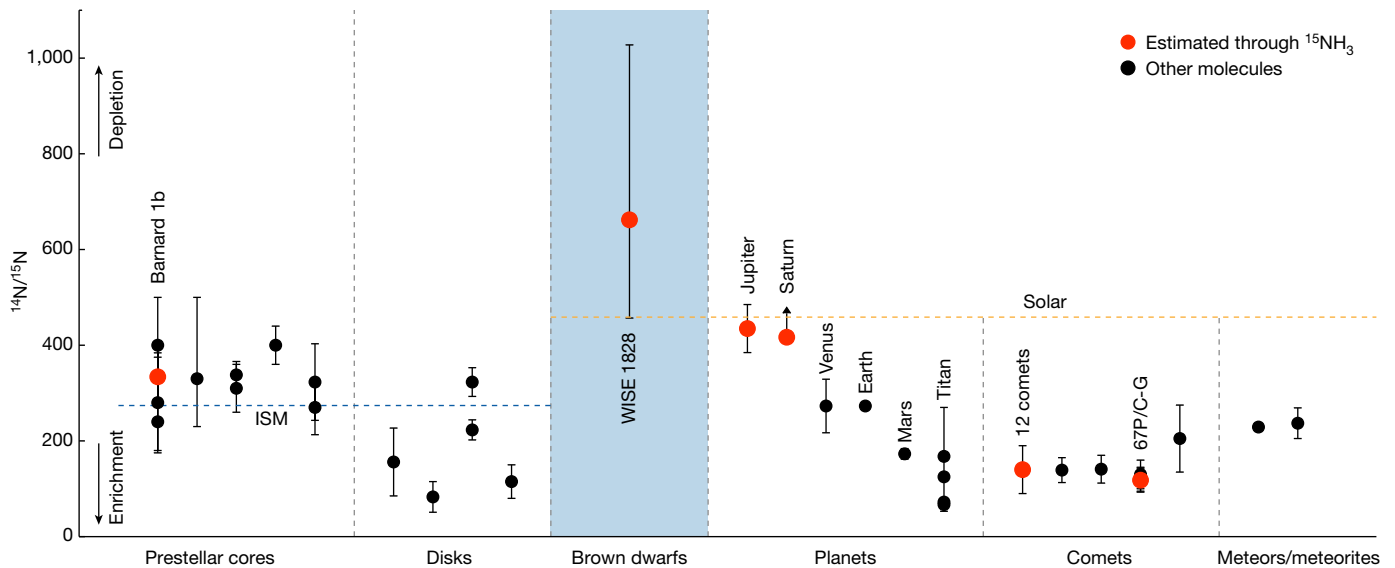


Fig. 2 | Comparison of the $^{14}\text{N}/^{15}\text{N}$ ratio in the solar neighbourhood. The values are based on either ammonia isotopologues (red circles) or other molecules (black symbols), in different environments, subdivided by classes⁷. Our estimate for WISE J1828 appears as the brown dwarf class and is consistent with solar

values (dashed yellow line) at the $1-2\sigma$ level. Other errors come from the cited compilation. Lower values indicate enrichment in ^{15}N , whereas the dashed blue line represents the current value of the ISM.

astrophysical objects⁷. Our value for WISE J1828 is consistent with solar at the $1-2\sigma$ level. Both the Sun and WISE J1828, which we derive to have similar ages, have $^{14}\text{N}/^{15}\text{N}$ values above those observed in the interstellar medium (ISM), which has been enriched in ^{15}N by galactic stellar

evolution since their formation¹⁰. Our measurement thus shows that WISE J1828 most probably formed like a star, as expected²⁷. A strong ice enrichment is unlikely and we correspondingly rule out cometary values $^{14}\text{N}/^{15}\text{N} < 200$ by more than 3σ .

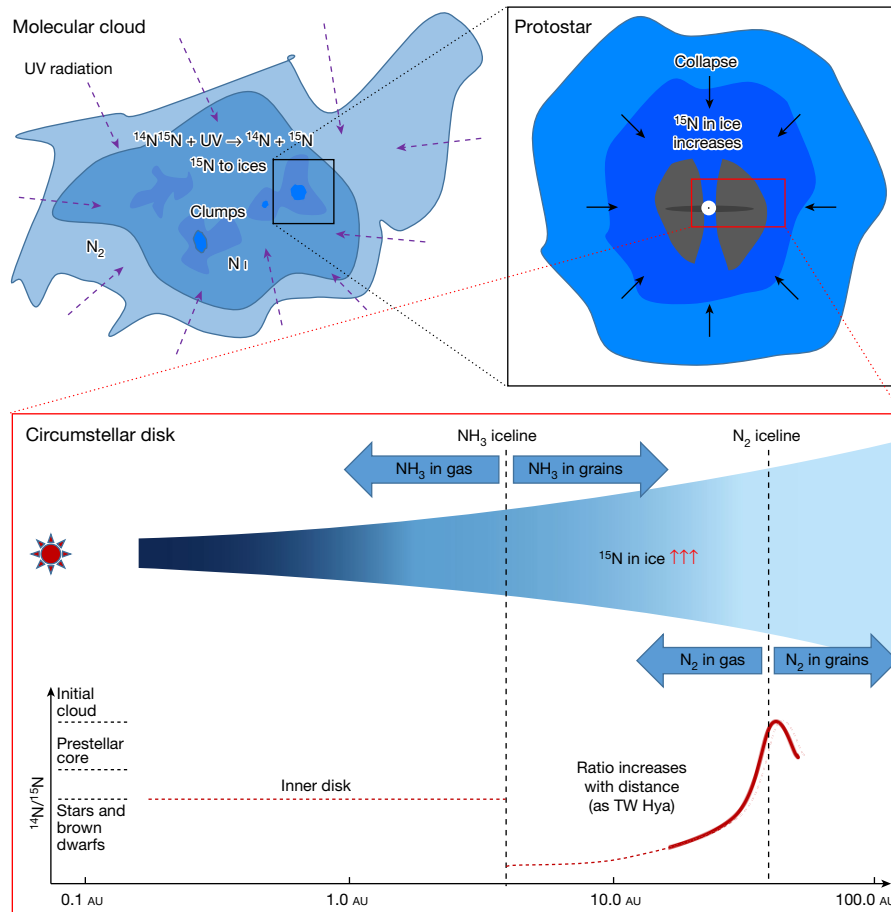


Fig. 3 | Different phases of star and planetary formation. We also show the relationship with the ammonia fractionation and the evolution of the $^{14}\text{N}/^{15}\text{N}$ ratio at these stages: inside a molecular cloud with prestellar cores, during the formation of a protostar and in a circumstellar disk around a young star.

Constraints on $^{14}\text{N}/^{15}\text{N}$ can serve as a formation tracer. For example, comets in the Solar System, fundamental planetary building blocks, are enriched in ^{15}N by a factor of 2–3 when compared with solar, owing to ^{15}N -rich NH_3 and HCN ice. By contrast, N_2 gas in the solar accretion disk is thought to have been depleted in ^{15}N (ref. 7). In the Solar System, both Jupiter and Saturn are enriched in bulk nitrogen but show $^{14}\text{N}/^{15}\text{N}$ values consistent with the Sun. This may mean that they accreted ice cold enough to contain even the volatile N_2 ice, which requires temperatures lower than 30 K, and corresponds to orbital distances greater than 25 AU (refs. 28,29). An enriched nitrogen content through accretion of ice, but at solar $^{14}\text{N}/^{15}\text{N}$, may therefore require accretion close to where even the highly volatile N_2 can condense.

The understanding of how nitrogen fractionation actually occurs is incomplete⁷, but we summarize some processes during different stages of the stellar and planetary evolution in Fig. 3. In the denser parts of the clouds, an increase of ^{15}N in NH_3 is inferred, with a candidate for this fractionation being isotope-selective photodissociation³⁰. Subsequently, NH_3 and HCN ices condense in the colder clumps, potentially producing ^{15}N -rich ice. Once a protostar is formed, there is some evidence that $^{14}\text{N}/^{15}\text{N}$ decreases further^{31,32}. The final consequence is thought to be a ^{15}N increase in the less volatile nitrogen carriers, leading to the observed increase in ^{15}N in HCN for protoplanetary disks and in NH_3 and HCN for Solar System comets. We note that models predict ^{15}N -poor NH_3 gas in protoplanetary disks³².

To further assess $^{14}\text{N}/^{15}\text{N}$ as a formation tracer, we used a simplified planet-formation model⁴. We tracked $^{14}\text{N}/^{15}\text{N}$ as a function of the mass accreted as icy and rocky material, for a planet located between the N_2 iceline of the disk, at about 20–80 AU, and the NH_3 iceline, ten times closer in^{29,33}. The ices were therefore probably enriched in ^{15}N . We find that, for Saturn-like metal enrichment (about six times solar³⁴), the $^{14}\text{N}/^{15}\text{N}$ decreases by 30–40% when compared with solar (see Extended Data Fig. 4), indicating that $^{14}\text{N}/^{15}\text{N}$ can vary substantially when compared with the stellar value for a planet forming between the N_2 and NH_3 icelines.

With the JWST MIRI, the formation-sensitive isotopologues $^{14}\text{NH}_3$ and $^{15}\text{NH}_3$ become accessible for objects with low effective temperatures. In the mid-infrared, NH_3 is a dominating absorber from $T_{\text{eff}} = 1,000$ K (ref. 35) down to at least 380 K, the effective temperature of WISE J1828. As demonstrated above, $^{14}\text{N}/^{15}\text{N}$ can constrain formation locations with respect to the NH_3 and N_2 icelines of the disk. This is as well as constraints on N/O, that the detection of H_2O and NH_3 enables, which has been suggested as another useful formation tracer^{36,37}, but which needs careful interpretation owing to chemical disequilibrium processes²⁵. Simultaneous constraints on C/O, N/O and $^{14}\text{N}/^{15}\text{N}$, based on CH_4 , CO , H_2O and NH_3 , can thus be obtained for cold directly imaged exoplanets, further explaining their formation history. These planets are found in orbits ranging from tens to hundreds of astronomical units, challenging the core-accretion model for planetary formation³⁸. They either formed at their detected locations by means of a star-like gravitational instability or originated closer to their star by means of core accretion and subsequent outward migration³⁹.

Online content

Any methods, additional references, Nature Portfolio reporting summaries, source data, extended data, supplementary information, acknowledgements, peer review information; details of author contributions and competing interests; and statements of data and code availability are available at <https://doi.org/10.1038/s41586-023-06813-y>.

- Burrows, A. et al. A nongray theory of extrasolar giant planets and brown dwarfs. *Astrophys. J.* **491**, 856–875 (1997).
- Faherty, J. K. in *Handbook of Exoplanets* (eds Deeg, H. & Belmonte, J.) 531–542 (Springer, 2018).
- Madhusudhan, N., Amin, M. A. & Kennedy, G. M. Toward chemical constraints on hot Jupiter migration. *Astrophys. J. Lett.* **794**, L12 (2014).
- Mollière, P. et al. Interpreting the atmospheric composition of exoplanets: sensitivity to planet formation assumptions. *Astrophys. J.* **934**, 74 (2022).

- Feuchtgruber, H. et al. The D/H ratio in the atmospheres of Uranus and Neptune from Herschel-PACS observations. *Astron. Astrophys.* **551**, A126 (2013).
- Alibert, Y. et al. The formation of Jupiter by hybrid pebble–planetesimal accretion. *Nat. Astron.* **2**, 873–877 (2018).
- Nomura, H. et al. The isotopic links from planet forming regions to the solar system. In *Protostars and Planets VII, ASP Conference Series* (eds Inutsuka, S.-i. et al.) Vol. 534 (Astronomical Society of the Pacific, 2023).
- Zhang, Y. et al. The ^{13}C -rich atmosphere of a young accreting super-Jupiter. *Nature* **595**, 370–372 (2021).
- Line, M. R. et al. A solar C/O and sub-solar metallicity in a hot Jupiter atmosphere. *Nature* **598**, 580–584 (2021).
- Adande, G. R. & Ziurys, L. M. Millimeter-wave observations of CN and HNC and their ^{15}N isotopologues: a new evaluation of the $^{14}\text{N}/^{15}\text{N}$ ratio across the galaxy. *Astrophys. J.* **744**, 194 (2012).
- Cushing, M. C. et al. The discovery of Y dwarfs using data from the Wide-field Infrared Survey Explorer (WISE). *Astrophys. J.* **743**, 50 (2011).
- Morley, C. V. et al. An L band spectrum of the coldest brown dwarf. *Astrophys. J.* **858**, 97 (2018).
- Skemer, A. J. et al. The first spectrum of the coldest brown dwarf. *Astrophys. J. Lett.* **826**, L17 (2016).
- Cushing, M. C. et al. An improved near-infrared spectrum of the archetype Y dwarf WISEP J182831.08+265037.8. *Astrophys. J.* **920**, 20 (2021).
- Beiler, S. A. et al. The first JWST spectral energy distribution of a Y dwarf. *Astrophys. J. Lett.* **951**, L48 (2023).
- Argyriou, I. et al. JWST MIRI flight performance: the Medium-Resolution Spectrometer. *Astron. Astrophys.* **675**, A111 (2023).
- Burningham, B. et al. Retrieval of atmospheric properties of cloudy L dwarfs. *Mon. Not. R. Astron. Soc.* **470**, 1177–1197 (2017).
- Mollière, P. et al. petitRADTRANS. A Python radiative transfer package for exoplanet characterization and retrieval. *Astron. Astrophys.* **627**, A67 (2019).
- Min, M., Ormel, C. W., Chubb, K., Helling, C. & Kawashima, Y. The ARCiS framework for exoplanet atmospheres. Modelling philosophy and retrieval. *Astron. Astrophys.* **642**, A28 (2020).
- Tremblin, P. et al. Fingering convection and cloudless models for cool brown dwarf atmospheres. *Astrophys. J. Lett.* **804**, L17 (2015).
- Chubb, K. L. & Min, M. Exoplanet atmosphere retrievals in 3D using phase curve data with ARCiS: application to WASP-43b. *Astron. Astrophys.* **665**, A2 (2022).
- De Furio, M. et al. JWST observations of the enigmatic Y-dwarf WISE 1828+2650. I. Limits to a binary companion. *Astrophys. J.* **948**, 92 (2023).
- Phillips, M. W. et al. A new set of atmosphere and evolution models for cool T–Y brown dwarfs and giant exoplanets. *Astron. Astrophys.* **637**, A38 (2020).
- Asplund, M., Grevesse, N., Sauval, A. J. & Scott, P. The chemical composition of the Sun. *Annu. Rev. Astron. Astrophys.* **47**, 481–522 (2009).
- Zahnle, K. J. & Marley, M. S. Methane, carbon monoxide, and ammonia in brown dwarfs and self-luminous giant planets. *Astrophys. J.* **797**, 41 (2014).
- Miles, B. E. et al. Observations of disequilibrium CO chemistry in the coldest brown dwarfs. *Astron. J.* **160**, 63 (2020).
- Chabrier, G., Johansen, A., Janson, M. & Rafikov, R. in *Protostars and Planets VI* (eds Beuther, H., Klessen, R. S., Dullemond, C. P. & Henning, T.) 619–642 (Univ. Arizona Press, 2014).
- Fletcher, L. N. et al. The origin of nitrogen on Jupiter and Saturn from the $^{15}\text{N}/^{14}\text{N}$ ratio. *Icarus* **238**, 170–190 (2014).
- Öberg, K. I. & Wordsworth, R. Jupiter's composition suggests its core assembled exterior to the N_2 snowline. *Astron. J.* **158**, 194 (2019).
- Furuya, K. & Aikawa, Y. Depletion of heavy nitrogen in the cold gas of star-forming regions. *Astrophys. J.* **857**, 105 (2018).
- Bergner, J. B., Öberg, K. I. & Bergin, E. A. et al. An evolutionary study of volatile chemistry in protoplanetary disks. *Astrophys. J.* **898**, 97 (2020).
- Visser, R. et al. Nitrogen isotope fractionation in protoplanetary disks. *Astron. Astrophys.* **615**, A75 (2018).
- Bosman, A. D., Cridland, A. J. & Miguel, Y. Jupiter formed as a pebble pile around the N_2 ice line. *Astron. Astrophys. Lett.* **632**, L11 (2019).
- Guillot, T. & Gautier, D. in *Treatise on Geophysics* (ed. Schubert, G.) 529–557 (Elsevier, 2015).
- Suarez, G. & Metchev, S. Ultracool dwarfs observed with the Spitzer infrared spectrograph – II. Emergence and sedimentation of silicate clouds in L dwarfs, and analysis of the full M5–T9 field dwarf spectroscopic sample. *Mon. Not. R. Astron. Soc.* **513**, 5701–5726 (2022).
- Öberg, K. I. & Bergin, E. A. Astrochemistry and compositions of planetary systems. *Phys. Rep.* **893**, 1–48 (2021).
- Turrini, D. et al. Tracing the formation history of giant planets in protoplanetary disks with carbon, oxygen, nitrogen, and sulfur. *Astrophys. J.* **909**, 40 (2021).
- Adams, F. C., Meyer, M. R. & Adams, A. D. A theoretical framework for the mass distribution of gas giant planets forming through the core accretion paradigm. *Astrophys. J.* **909**, 1 (2021).
- Marleau, G.-D., Coleman, G. A. L., Leleu, A. & Mordasini, C. Exploring the formation by core accretion and the luminosity evolution of directly imaged planets. The case of HIP 65426 b. *Astron. Astrophys.* **624**, A20 (2019).

Publisher's note Springer Nature remains neutral with regard to jurisdictional claims in published maps and institutional affiliations.

Springer Nature or its licensor (e.g. a society or other partner) holds exclusive rights to this article under a publishing agreement with the author(s) or other rightsholder(s); author self-archiving of the accepted manuscript version of this article is solely governed by the terms of such publishing agreement and applicable law.

© The Author(s), under exclusive licence to Springer Nature Limited 2023

Methods

JWST MIRI observations and data processing

The MIRI/MRS targeted WISE J1828 on 28 July 2022 without the use of target acquisition as part of JWST Guaranteed Time Observing programme with PID 1189. All three dichroic/grating settings (SHORT, MEDIUM, LONG) were obtained to cover the full wavelength range, from 4.9 to 27.9 μm (ref. 16). The observations were executed with the point-source-optimized two-point dither (negative direction) and the detector set up with 180 frames per integration. No dedicated background observations were obtained.

The JWST pipeline was used (pipeline version: 1.9, CRDS version: 11.16.20, CRDS context: jwst_1045.pmap) to process the data. The raw (level 1B) files were processed with the detector-level pipeline (CALWEBB_DETECTOR1) to produce calibrated rate files. This pipeline applies corrections for the nonlinearity of the ramps, dark current, detects jumps in the ramp resulting from cosmic rays and, finally, fits the ramp signal to obtain slope values (rate.fits). The detector images were inspected and no sign of cosmic-ray showers were found¹⁶. Because the WISE J1828 detector images were clean, we could use the fact that the point source itself is faint to perform a nod subtraction between the two dither points. First, we had to make sure that, for every pair of detector images, the flux levels were on the same level before subtracting them. A small time-dependent difference between the individual integrations has been seen in MRS observations, with the first integration of the visit having a brighter flux level originating from the detector idling before the start of the exposures¹⁶. We used the region between the MRS channels on the detectors that do not contain any astrophysical signal to estimate a single value using the median and subtract it from the whole detector. Next, the two dithers were subtracted from each other to remove the thermal background contribution. For Channel 1 of the MRS, a detector artefact that manifests as vertical stripes was still present after the nod subtraction. These stripes were around 10% of the science signal and, because the dispersion direction also closely follows the detector columns¹⁶, the stripes affect the continuum of the extracted spectrum. We chose a region of the detector in which the source signal was almost zero and estimated the stripe contribution as the median of ten rows, which was then subtracted from every row of the detector.

With the detector images clean from detector artefacts and the thermal background, the spectroscopy pipeline (CALWEBB_SPEC2) was run to obtain calibrated detector images (cal.fits), assigning the astrometric and wavelength information, correcting for the scattered light and detector fringing, and applying the photometric calibration. Finally, with CALWEBB_SPEC3, we built the dither combined cubes⁴⁰, with outlier rejection enabled. With background-subtracted cubes, the spectral extraction from the cube is done by performing aperture photometry for each wavelength slice of the cube. We first determined the centre of the point source by fitting a 2D Gaussian in the wavelength-collapsed cube, then placed an aperture of one full width at half maximum centred on the source, applying an aperture correction for each wavelength to account for the missing flux of the point-spread function outside the aperture. Some outliers remain in the extracted spectrum, which were removed for plotting the spectrum in Fig. 1 but not while fitting it. We traced back these outliers to the detector, at which a few cosmic rays overlap with the spectral trace but are not bright enough for the outlier algorithm to detect. We therefore clip these values manually for each spectral band by setting a threshold for the flux. The outliers affected in total 0.4% of the spectrum.

Retrieval analysis

We carried out independent analyses of the MIRI/MRS spectra using a diversity of models, namely, with the radiative-convective equilibrium codes ATMO and ARCIS+ML, and with the retrieval codes ARCIS, Brewster and petitRADTRANS (refs. 17–21 and F.A.M. et al., manuscript in

preparation). For computational feasibility, the retrievals with ARCIS, Brewster and petitRADTRANS were run at a resolution of $\lambda/\Delta\lambda = 1,000$; the MRS data were binned down correspondingly. For the retrievals, we decided on a setup that assumed vertically constant absorber abundances that were retrieved freely and a flexible parameterization of the pressure–temperature (P – T) structure, which varied slightly between the setups; see below. For the retrievals presented here, we assumed WISE J1828 to be a single object but allowed for a radius prior wide enough to account for an equal-brightness binary scenario. Clouds were neglected, which seems to be justified from a population-wide Y-dwarf retrieval analysis on Hubble Space Telescope (HST) data⁴¹. We note, however, that the impact of clouds should increase towards longer wavelengths and for colder Y dwarfs^{12,42}. As shown in Extended Data Fig. 2, our inferred P – T profiles cross the water saturation vapour pressure curve at the top of the photosphere examined by the HST and the MIRI, so a cloud could have some moderate impact on our results and the effect of its inclusion should be assessed in future studies.

We also observed that the reported uncertainties of the JWST reduction can be much smaller than the differences observed in the overlapping regions of MRS subchannels. Also, all best-fit models had a χ^2 considerably larger than the number of wavelength channels. We thus opted for retrieving the magnitude of the uncertainties through the 10^b treatment⁴³, in which the error bars σ considered during the retrieval are calculated from the uncertainties reported from the reduction σ_{red} as follows: $\sigma = \sqrt{\sigma_{\text{red}}^2 + 10^b}$. Separate b s were retrieved for MIRI and HST data. The retrieved P – T structures of the retrievals would also exhibit kinks sometimes, which are challenging to reconcile with radiative-convective equilibrium models. In this case, we implemented a regularization of the P – T structure⁴³. With this modification, the ARCIS and petitRADTRANS retrievals optionally put a penalty on $d^2\log T/d\log P^2$, which strives towards a constant power-law dependence between pressure and temperature, as $d\log T/d\log P = \text{constant}$ implies $T \propto P^\alpha$, with α being the constant power-law coefficient. This setup may therefore also reproduce the relation between pressure and temperature in the deep atmosphere, which is expected to be convective. The individual models we used for the analysis are described below.

The results of all model inferences for WISE J1828 are found in Extended Data Table 1 and the combined result of all retrievals is presented in Extended Data Table 2. Elemental abundance ratios (C/O, N/O, $^{14}\text{N}/^{15}\text{N}$) were computed from the VMR constraints of the retrievals for the atmospheric absorbers. They may thus miss further atoms locked up in clouds (in the case of oxygen) or affected by quenching in species that are spectrally inactive (N_2 in the case of N) or have features outside the HST and MIRI wavelength range (CO in the case of C and O). The one-dimensional projection of the posteriors, for key forward model parameters, is shown in Extended Data Fig. 3 for all individual models. In Extended Data Fig. 2, we show the associated P – T uncertainties derived from all model analyses.

ATMO. We briefly describe the main properties of the ATMO²⁰ models and the grids that have been used in our study. These grids are publicly available at <https://opendata.erc-atmo.eu>. The ATMO models assume that clouds are not needed to reproduce the shape of the spectral energy distribution of brown dwarfs (apart from the 10- μm silicate feature). The authors have proposed that diabatic convective processes⁴⁴ induced by out-of-equilibrium chemistry of CO/CH₄ and N₂/NH₃ can reduce the temperature gradient in the atmosphere and reproduce the reddening previously thought to occur by clouds. The grids assume a modification of the temperature gradient with an effective adiabatic index. The levels modified are between 2 and 200 bar at $\log(g) = 5.0$ and are scaled by $10^{\log(g)-5}$ at other surface gravities. Out-of-equilibrium chemistry is used with $K_{zz} = 10^5 \text{ cm}^2 \text{ s}^{-1}$ at $\log(g) = 5.0$ and is scaled by $10^{2[5-\log(g)]}$ at other surface gravities. The mixing length is assumed to be two scale heights at 20 bar and higher pressures at $\log(g) = 5.0$, and is scaled down by the ratio between the local pressure and the

Article

pressure at 20 bar for lower pressures. The 20-bar limit is scaled by $10^{\log(g)-5}$ at other surface gravities. The chemistry includes 277 species and out-of-equilibrium chemistry has been performed using a relaxation model⁴⁵. Rainout is assumed to occur for species that are not included in the out-of-equilibrium model. Opacity sources include H_2 - H_2 , H_2 -He, H_2O , CO_2 , CO , CH_4 , NH_3 , Na, K, Li, Rb, Cs, TiO, VO, FeH, PH_3 , H_2S , HCN, C_2H_2 , SO_2 , Fe, H- and the Rayleigh scattering opacities for H_2 , He, CO, N_2 , CH_4 , NH_3 , H_2O , CO_2 , H_2S and SO_2 . The grids explore the following parameters: effective temperatures between 250 and 1,200 K; $\log(g)$ between 2.5 and 5.5 (step 0.5); effective adiabatic index (reddening) at a value of 1.25. A standard χ^2 -minimization procedure was used to find the best-fitting model.

petitRADTRANS. petitRADTRANS, or pRT (ref. 18, available from <https://petitradtrans.readthedocs.io>), is a Python package for the spectral synthesis of exoplanets and allows users to calculate transmission, emission or reflectance spectra. It offers a wide selection of opacities (gas line and continuum, and cloud opacities). Spectra can be calculated at any resolution, up to a wavelength spacing of $\lambda/\Delta\lambda = 10^6$. Coupled to a Bayesian inference method such as PyMultiNest^{46,47}, which petitRADTRANS provides as a pre-implemented retrieval package, posterior distributions for atmospheric parameters can be derived, given an observation. For WISE J1828, we assumed a forward model setup as described for the retrievals above, with the priors and forward model details set up as described in the following. The prior on $\log(g)$ was uniform from 2.5 to 6.0, whereas the radius prior ranged from 0.5 to 3.0 Jupiter radii. Also, the P - T profile was parameterized by retrieving temperature values at ten locations, equidistantly spaced in log-space between 10^{-6} and 1,000 bar, and then quadratically interpolating the temperature between these nodes in log(pressure). The priors were set up such that the temperature at 1,000 bar was uniformly sampled between 100 and 9,000 K, and the temperatures at lower-pressure nodes was allowed to be between 0.2 and 1.0 times the temperature of the neighbouring deeper atmospheric node. Because kinks in the P - T profiles could be observed in the standard setup, the P - T regularization described above was optionally turned on when deriving the atmospheric model posteriors, fitting both MIRI/MRS and the archival HST WFC3 data. Our constraints on $^{14}\text{N}/^{15}\text{N}$ are not affected by the regularization. However, we observed a trend that a regularized P - T leads to a higher atmospheric metal enrichment, higher gravity $\log(g)$, smaller radii and higher effective temperatures (see Extended Data Fig. 2). For the detection of $^{15}\text{NH}_3$, we only used the MRS data. We also turned the regularization off to allow for maximum model flexibility. This leads to a conservative estimate of the detection significance. The following opacity species were included in the retrievals: H_2O (ref. 48), CH_4 (ref. 49), CO (ref. 50), CO_2 (ref. 51), $^{15}\text{NH}_3$ (ref. 52), H_2S (ref. 53), NH_3 (ref. 54) and PH_3 (ref. 55). The abundances of said molecules were retrieved using log-uniform priors from 10^{-10} to 1 on their mass fractions. For the $^{15}\text{NH}_3$ detection, we used PyMultiNest, with 2,000 live points, constant_sampling_efficiency set to false and a sampling efficiency of 0.3. The detection significance of $^{15}\text{NH}_3$ was determined using a standard method⁴⁵. We report a detection significance of 4.2σ for $^{15}\text{NH}_3$. For the retrievals constraining the properties of WISE J1828, which included HST as well as MRS data, we ran in constant sampling efficiency mode, with the efficiency set to 5%. This needed to be done because, otherwise, retrievals ran for 10^8 models but did not finish. The partially filled weighted posterior files of the 10^8 model retrievals were consistent with the results using the constant sampling efficiency mode. With petitRADTRANS, we found $^{14}\text{N}/^{15}\text{N} = 560_{-115}^{+165}$ for the flexible P - T model and $^{14}\text{N}/^{15}\text{N} = 642_{-192}^{+365}$ for the regularized P - T model.

ARCiS. The ARTfull Modeling Code for exoplanet Science (ARCiS) is a forward modelling and retrieval code that can be used to analyse and simulate exoplanet atmosphere spectra. It contains many physical and

chemical processes, including cloud formation⁵⁷ and disequilibrium chemistry⁵⁸. The free P - T structure used in this work is parameterized by the slope at several pressure points in the atmosphere. We parameterize $d\log T/d\log P$ with a prior range between $-4/7$ and $+4/7$. The adiabatic gradient expected for a diatomic gas is $d^2\log T/d\log P^2 = 2/7$, so this prior range gives a very generous range. We fix the absolute value of the temperature structure at a pressure of $P = 0.1$ bar. We retrieve the value of the slope at 12 pressure points distributed equally over the atmosphere in $\log(-P)$ space. For the detection of $^{15}\text{NH}_3$, we follow this procedure, allowing full flexibility and thereby constructing a conservative detection significance. For the final fits deriving the isotopic ratio and the planet parameters presented, we restrict the gradient of the P - T structure to be positive, as expected for a non-irradiated atmosphere. Following a standard approach⁵⁶, we find evidence that $^{15}\text{NH}_3$ is present in the atmosphere of WISE J1828 at 6.3σ . We observe the same trend between metal enrichment, $\log(g)$, radii and effective temperature as petitRADTRANS when regularizing the P - T structure (see Fig. 2). However, our derived $^{14}\text{N}/^{15}\text{N}$ values are less stable when turning on regularization. Our regularized values are consistent with petitRADTRANS (regularized and flexible P - T), namely, $^{14}\text{N}/^{15}\text{N} = 591_{-190}^{+432}$. The value derived for the flexible P - T setup is higher ($^{14}\text{N}/^{15}\text{N} = 949_{-208}^{+323}$). More information on ARCiS can be found at <http://www.exoclouds.com>.

ARCiS+ML. For the self-consistent retrieval with ARCiS, we assume a one-dimensional atmosphere in radiative-convective equilibrium. The retrievals were run on the MIRI MRS data only (that is, not including the HST data). The atmospheric composition is parameterized using $[\text{M}/\text{H}]$, C/O and N/O and we account for disequilibrium chemistry of CH_4 - H_2O - CO and NH_3 - N_2 owing to vertical mixing⁵⁸, in which the vertical eddy diffusion coefficient K_{zz} is another free parameter. For WISE J1828, we observed that, although NH_3 - N_2 quenching was active in our models, it quenched from the lowest layer in the atmosphere, in which NH_3 was still the dominating absorber. Probably quenching actually occurs outside our simulated pressure domain, deeper inside the atmosphere. Therefore, the ARCiS+ML constraints may be too low for N/O , similar to the constraints from the retrievals, which are insensitive to the spectrally inactive N_2 . The radiative transfer module was benchmarked²¹. Owing to the high computational load of the self-consistent models, we cannot run nested sampling retrievals, which require millions of model evaluations to converge. Instead, we use a machine-learning method based on sequential neural posterior estimation (SNPE)⁵⁹ that allows us to perform the retrieval using on the order of 10^4 models. The details of this retrieval method will be presented in an upcoming publication (F.A.M. et al., manuscript in preparation).

Brewster. Brewster^{17,60} is a retrieval code that has mainly been used in the context of exploring clouds in brown dwarfs. However, here, we used a simple, cloud-free retrieval recipe. Brewster uses the two-stream radiative-transfer architecture⁶¹. We use the default 64-layer atmosphere with intervals of 0.1 dex across the pressures range $\log P(\text{bar})$ of -4 to 2.3. The temperature is set using P - T parameterization⁶² linked to three atmospheric zones by means of exponential gradients. We included the molecules H_2O , CH_4 , NH_3 , CO , PH_3 and H_2S , which originate from a compendium^{63,64} and updated opacities¹⁷. The abundances of these molecules are modelled assuming vertically constant mixing ratios, which are retrieved as free parameters. The opacities are ingested at a resolution of $R = 10,000$, putting the native model resolution an order of magnitude above the data being fit. Continuum opacities for H_2 - H_2 and H_2 -He collisionally induced absorption, Rayleigh scattering owing to H_2 , He and CH_4 , and continuum opacities owing to bound-free and free-free absorption by H- and free-free absorption by H_2 are also included. We apply an error inflation ‘tolerance’ framework⁴³ and used in all subsequent published works using Brewster. Only the JWST/MIRI

MRS observations were retrieved with Brewster, so the HST data were not included. Here we used the emcee⁶⁵ as our sampling algorithm. As we used the standard retrieval recipe for this code, an extensive list of parameter sampling priors has been used⁶⁰.

Combining model results

Whenever we report values for the properties of WISE J1828 in the main body of the text, these have been obtained from combining the posteriors of the retrievals at equal weight and calculating the corresponding median and 16th–84th percentile values, corresponding to the 1 σ credible interval in the case that the resulting distribution is approximately Gaussian. The combined value of the self-consistent codes was obtained by taking the average of their best-fit (ATMO) and median (ARCI+ML) values, whereas the uncertainty is obtained from calculating the difference d between these two values and then calculating $\sqrt{d^2 + a^2}$, in which a is the '1 σ ' uncertainty obtained from the ARCI+ML posterior.

Exploring ¹⁴N/¹⁵N as a formation tracer

To approximate the impact of volatile ice accretion between the NH₃ and N₂ icelines in a protoplanetary disk, we generated a simplified planet-formation model for calculating ¹⁴N/¹⁵N as a function of the total solid mass (rock and ices) a planet incorporated during formation. For this, we used a specific framework⁴, which is available at <https://gitlab.com/mauricemolli/formation-inversion>. In short, we used a solar disk composition (Table 2 in ref. 4). This means that the mass ratio between NH₃ and N₂ is 1:7 in the disk (combining gas and ice reservoirs). We then assumed, conservatively, that ¹⁴N/¹⁵N is reduced by a factor of 2 in NH₃ when compared with the total ¹⁴N/¹⁵N value, whereas the total ¹⁴N/¹⁵N (summing over all species and phases) is conserved, which we assumed to be 300, and call the ISM value in Extended Data Fig. 4. This figure shows the ratio of the planetary and ISM values of ¹⁴N/¹⁵N as a function of solids accreted by a planet between the NH₃ and N₂ icelines. Because the solids are rich in NH₃ and N₂ is only in the gas phase, a higher accreted solid mass results in a lower planetary ¹⁴N/¹⁵N. We note that the picture could be more complicated, as the disk gas could be enriched in ¹⁵N-poor N₂ gas that evaporated off pebbles that drift in from outside the N₂ iceline⁶⁶.

Inclusion and ethics

All authors have committed to upholding the principles of research ethics and inclusion as advocated by the Nature Portfolio journals.

Data availability

The JWST MIRI data presented in this paper are part of the JWST MIRI GTO programme (programme identifier (PID) 1189; PI T. Roellig). The JWST data will be publicly available in the Barbara A. Mikulski Archive for Space Telescopes (MAST; <https://archive.stsci.edu/>) after 28 July 2023 and can be found either using the programme identifier or using the <https://doi.org/10.17909/as3s-x893>. The HST WFC3 spectrum is available from <https://cdsarc.cds.unistra.fr/viz-bin/cat/J/ApJ/920/20#/article>.

Code availability

The code used in this publication to extract, reduce and analyse the data is as follows: the data-reduction pipeline of JWST can be found at <https://jwst-pipeline.readthedocs.io/en/latest/>; the atmospheric model codes used to fit the data can be found at <https://www.exoclouds.com/> for the ARCI code¹⁹ and at <https://petitradtrans.readthedocs.io/en/latest/> for the petitRADTRANS code¹⁸. The simplified planet-formation model⁴ used to study ¹⁴N/¹⁵N as a function of accreted ice mass can be found at <https://gitlab.com/mauricemolli/formation-inversion>. The detailed setups of the open-source tools for the analyses presented

here are described in the Methods section of this paper and can be made available to interested parties on request.

40. Law, D. R. et al. A 3D drizzle algorithm for JWST and practical application to the MIRI Medium Resolution Spectrometer. *Astron. J.* **166**, 45 (2023).
41. Zalesky, J. A., Line, M. R., Schneider, A. C. & Patience, J. A uniform retrieval analysis of ultra-cool dwarfs. III. Properties of Y dwarfs. *Astrophys. J.* **877**, 24 (2019).
42. Mang, J. et al. Microphysics of water clouds in the atmospheres of Y dwarfs and temperate giant planets. *Astrophys. J.* **927**, 184 (2022).
43. Line, M. R., Teske, J., Burningham, B., Fortney, J. J. & Marley, M. S. Uniform atmospheric retrieval analysis of ultracool dwarfs. I. Characterizing benchmarks, Gl 570D and HD 3651B. *Astrophys. J.* **807**, 183 (2015).
44. Tremblin, P. et al. Thermo-compositional diabatic convection in the atmospheres of brown dwarfs and in Earth's atmosphere and oceans. *Astrophys. J.* **876**, 144 (2019).
45. Tsai, S.-M. et al. VULCAN: an open-source, validated chemical kinetics Python code for exoplanetary atmospheres. *Astrophys. J. Suppl. Ser.* **228**, 20 (2017).
46. Feroz, F. & Feroz, M. P. Multimodal nested sampling: an efficient and robust alternative to Markov Chain Monte Carlo methods for astronomical data analyses. *Mon. Not. R. Astron. Soc.* **384**, 449–463 (2008).
47. Buchner, J. et al. X-ray spectral modelling of the AGN obscuring region in the CDFS: Bayesian model selection and catalogue. *Astron. Astrophys.* **564**, A125 (2014).
48. Polyansky, O. L. et al. ExoMol molecular line lists XXX: a complete high-accuracy line list for water. *Mon. Not. R. Astron. Soc.* **480**, 2597–2608 (2018).
49. Hargreaves, R. J. et al. An accurate, extensive, and practical line list of methane for the HITEMP database. *Astrophys. J. Suppl. Ser.* **247**, 55 (2020).
50. Rothman, L. S. et al. HITEMP, the high-temperature molecular spectroscopic database. *J. Quant. Spectrosc. Radiat. Transfer* **111**, 2139–2150 (2010).
51. Yurchenko, S. N., Mellor, T. M., Freedman, R. S. & Tennyson, J. ExoMol line lists – XXXIX. Ro-vibrational molecular line list for CO₂. *Mon. Not. R. Astron. Soc.* **496**, 5282–5291 (2020).
52. Rothman, L. S. et al. The HITRAN2012 molecular spectroscopic database. *J. Quant. Spectrosc. Radiat. Transfer* **130**, 4–50 (2013).
53. Azzam, A. A. A., Tennyson, J., Yurchenko, S. N. & Naumenko, O. V. ExoMol molecular line lists – XVI. The rotation–vibration spectrum of hot H₂S. *Mon. Not. R. Astron. Soc.* **460**, 4063–4074 (2016).
54. Coles, P. A., Yurchenko, S. N. & Tennyson, J. ExoMol molecular line lists – XXXV. A rotation–vibration line list for hot ammonia. *Mon. Not. R. Astron. Soc.* **490**, 4638–4647 (2019).
55. Sousa-Silva, C., Al-Refaie, A. F., Tennyson, J. & Yurchenko, S. N. ExoMol line lists – VII. The rotation–vibration spectrum of phosphine up to 1500 K. *Mon. Not. R. Astron. Soc.* **446**, 2337–2347 (2014).
56. Benneke, B. & Seager, S. How to distinguish between cloudy mini-Neptunes and water/volatile-dominated super-Earths. *Astrophys. J.* **778**, 153 (2013).
57. Ormel, C. W. & Min, M. ARCI framework for exoplanet atmospheres. The cloud transport model. *Astron. Astrophys.* **622**, A121 (2019).
58. Kawashima, Y. & Min, M. Implementation of disequilibrium chemistry to spectral retrieval code ARCI and application to 16 exoplanet transmission spectra. Indication of disequilibrium chemistry for HD 209458b and WASP-39b. *Astron. Astrophys.* **656**, A90 (2021).
59. Greenberg, D., Nonnenmacher, M. & Macke, J. in *Proc. 36th International Conference on Machine Learning* Vol. 97 (eds Chaudhuri, K. & Salakhutdinov, R.) 2404–2414 (PMLR, 2019).
60. Burningham, B. et al. Cloud busting: enstatite and quartz clouds in the atmosphere of 2M2224-0158. *Mon. Not. R. Astron. Soc.* **506**, 1944–1961 (2021).
61. Toon, O. B., McKay, C. P., Ackerman, T. P. & Santhanam, K. Rapid calculation of radiative heating rates and photodissociation rates in inhomogeneous multiple scattering atmospheres. *J. Geophys. Res. Atmos.* **94**, 16287–16301 (1989).
62. Madhusudhan, N. & Seager, S. A temperature and abundance retrieval method for exoplanet atmospheres. *Astrophys. J.* **707**, 24–39 (2009).
63. Freedman, R. S., Marley, M. S. & Lodders, K. Line and mean opacities for ultracool dwarfs and extrasolar planets. *Astrophys. J. Suppl. Ser.* **174**, 504–513 (2008).
64. Freedman, R. S. et al. Gaseous mean opacities for giant planet and ultracool dwarf atmospheres over a range of metallicities and temperatures. *Astrophys. J. Suppl. Ser.* **214**, 25 (2014).
65. Foreman-Mackey, D., Hogg, D. W., Lang, D. & Goodman, J. emcee: the MCMC hammer. *Publ. Astron. Soc. Pac.* **125**, 306 (2013).
66. Schneider, A. D. & Bitsch, B. How drifting and evaporating pebbles shape giant planets. II. Volatiles and refractories in atmospheres. *Astron. Astrophys.* **654**, A72 (2021).

Acknowledgements This work is based (in part) on observations made with the NASA/ESA/CSA James Webb Space Telescope (JWST). The data were obtained from the Mikulski Archive for Space Telescopes (MAST) at the Space Telescope Science Institute, which is operated by the Association of Universities for Research in Astronomy, Inc., under NASA contract NAS 5-03127 for the JWST. These observations are associated with programme 1189. The Mid-Infrared Instrument (MIRI) draws on the scientific and technical expertise of the following organizations: Ames Research Center, USA; Airbus Defence and Space, UK; CEA/IRFU, Saclay, France; Centre Spatial de Liège, Belgium; Consejo Superior de Investigaciones Científicas, Spain; Carl Zeiss Optronics, Germany; Chalmers University of Technology, Sweden; Danish Space Research Institute, Denmark; Dublin Institute for Advanced Studies, Ireland; European Space Agency, the Netherlands; ETCA, Belgium; ETH Zurich, Switzerland; Goddard Space Flight Center, USA; Institut d'Astrophysique Spatiale, France; Instituto Nacional de Técnica Aeroespacial, Spain; Institute for Astronomy, Edinburgh, UK; Jet Propulsion Laboratory, USA; Laboratoire d'Astrophysique de Marseille (LAM), France; Leiden University, the Netherlands; Lockheed Advanced Technology Center, USA; NOVA Opt-IR Group at Dwingeloo, the Netherlands; Northrop Grumman, USA; Max-Planck-Institut für Astronomie (MPIA), Heidelberg, Germany; Laboratoire d'Etudes Spatiales et d'Instrumentation en Astrophysique (LESIA), France; Paul Scherrer Institut, Switzerland; Raytheon Vision Systems, USA; RUAG Aerospace, Switzerland;

Article

Rutherford Appleton Laboratory (RAL Space), UK; Space Telescope Science Institute, USA; Toegepast Natuurwetenschappelijk Onderzoek (TNO-TPD), the Netherlands; UK Astronomy Technology Centre, UK; University College London, UK; University of Amsterdam, the Netherlands; University of Arizona, USA; University of Bern, Switzerland; University of Cardiff, UK; University of Cologne, Germany; University of Ghent, Belgium; University of Groningen, the Netherlands; University of Leicester, UK; KU Leuven, Belgium; University of Stockholm, Sweden; and Utah State University, USA. The following national and international funding agencies funded and supported the MIRI development: NASA; ESA; Belgian Science Policy Office (BELSPO); Centre Nationale d'Etudes Spatiales (CNES); Danish National Space Center; Deutsches Zentrum für Luft und Raumfahrt (DLR); Enterprise Ireland; Ministerio de Economía y Competitividad; Netherlands Research School for Astronomy (NOVA); Netherlands Organisation for Scientific Research (NWO); Science and Technology Facilities Council; Swiss Space Office; Swedish National Space Agency; and UK Space Agency. D.B. and M.M.-C. are supported by Spanish MCIN/AEI/10.13039/501100011033 grant nos. PID2019-107061GB-C61 and MDM-2017-0737. C.C., A.B., P.-O.L., R.G. and A.C. acknowledge funding support from CNES. P.P. thanks the Swiss National Science Foundation (SNSF) for financial support under grant number 200020_200399. N.W. acknowledges funding from NSF award 1909776 and NASA XRP award 80NSSC22K0142. O.A., I.A., B.V. and P.R. thank the European Space Agency (ESA) and the Belgian Science Policy Office (BELSPO) for their support in the framework of the PRODEX Programme. L.D. acknowledges funding from the KU Leuven Interdisciplinary Grant (IDN/19/028), the European Union H2020-MSCA-ITN-2019 under grant no. 860470 (CHAMELEON) and the FWO research grant G086217N. I.K. acknowledges support from grant TOP-1 614.001.751 from the Dutch Research Council (NWO). O.K. acknowledges support from the Federal Ministry of Economy and Energy (BMWi) through the German Space Agency (DLR). J.P. acknowledges financial support from the UK Science and Technology Facilities Council and the UK Space Agency. G.O. acknowledges support from the Swedish National Space Board and the Knut and Alice Wallenberg Foundation. P.T. acknowledges support by the European Research Council (ERC) under grant agreement ATMO 757858. F.A.M. has received funding from the European Union's Horizon 2020 research and innovation programme under the Marie Skłodowska-Curie grant agreement no. 860470. L.C. acknowledges support by grant PIB2021-127718NB-100 from the Spanish Ministry of Science and Innovation/State Agency of Research MCIN/AEI/10.13039/501100011033. E.F.v.D. acknowledges support from A-ERC grant 101019751 MOLDISK. T.R. acknowledges support from the ERC 743029 EASY. G.Ö. acknowledges support from SNSA.

T.H. acknowledges support from the ERC under the European Union's Horizon 2020 research and innovation programme under grant agreement no. 832428-Origins. We thank the MIRI instrument team and the many others who contributed to the success of the JWST.

Author contributions All authors played a substantial role in one or more of the following: designing and building the MIRI, development of the original proposal, management of the project, definition of the target list and observation plan, analysis of the data, theoretical modelling and preparation of this paper. Some specific contributions are listed as follows. P.-O.L. is PI of the JWST MIRI GTO European consortium programme dedicated to JWST observations of exoplanet atmospheres. D.B., P.M. and P.P. provided overall programme leadership and management of the WISE J1828 working group. P.-O.L., T.H., R.W., (co-lead of the JWST MIRI GTO European consortium), D.B. and M.Mu. made notable contributions to the design of the observational programme and contributed to the setting of the observing parameters. P.P., I.A. and M.S. reduced the data. P.T. generated theoretical model grids for comparison with the data. P.M., M.Mi. and N.W. fitted the generated spectrum with retrieval models and M.V. also contributed. F.A.M. applied the radiative-convective equilibrium retrieval to the spectrum. D.B., P.M. and P.P. led the writing of the manuscript. P.-O.L. and L.D. made notable contributions to the writing of this paper. Further contributions were provided by M.M.-C. and L.D. P.B., A.B., J.B., C.C., A.C., N.C., R.G., A.G., A.M.G., S.K., F.L., D.R., P.R., S.S. and I.W. contributed to instrument construction, the programme design and/or the data analysis. P.M., P.P. and D.B. generated the figures for this paper. G.W. is PI of the JWST MIRI instrument, P.-O.L., T.H., M.G., B.V., L.C., E.F.v.D., T.R. and G.Ö. are co-PIs and L.D., R.W., O.A., I.K., O.K., J.P., G.O. and D.B. are co-investigators of the JWST MIRI instrument.

Competing interests The authors declare no competing interests.

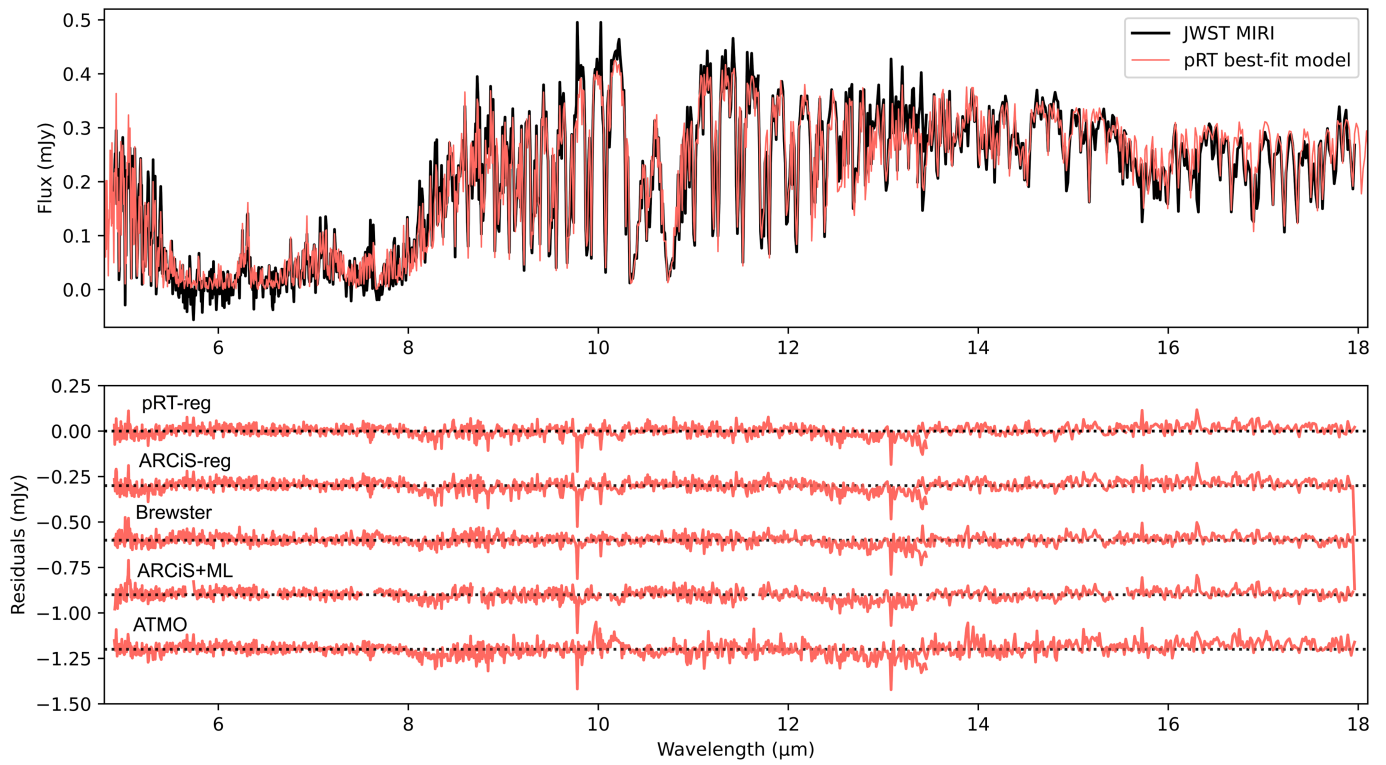
Additional information

Supplementary information The online version contains supplementary material available at <https://doi.org/10.1038/s41586-023-06813-y>.

Correspondence and requests for materials should be addressed to David Barrado.

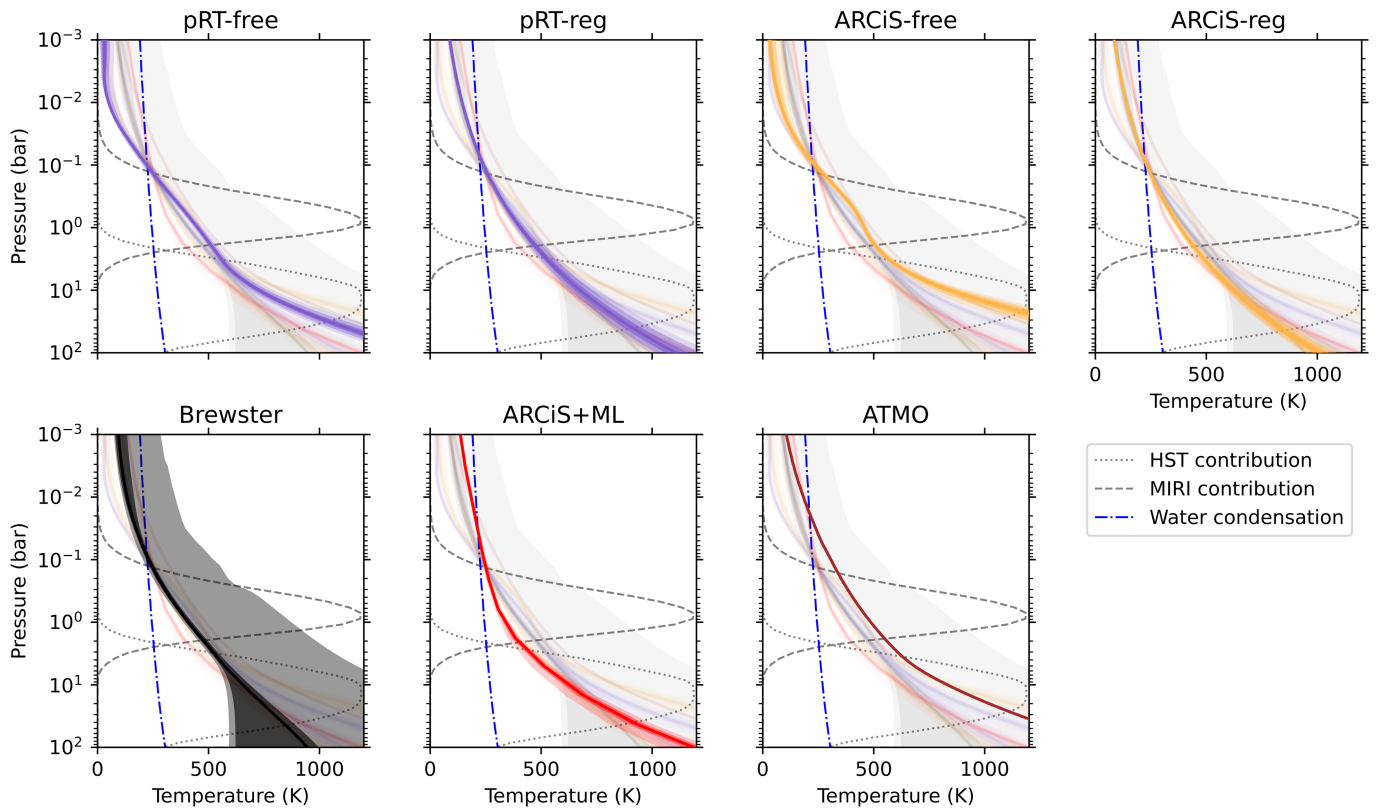
Peer review information *Nature* thanks the anonymous reviewers for their contribution to the peer review of this work. Peer reviewer reports are available.

Reprints and permissions information is available at <http://www.nature.com/reprints>.



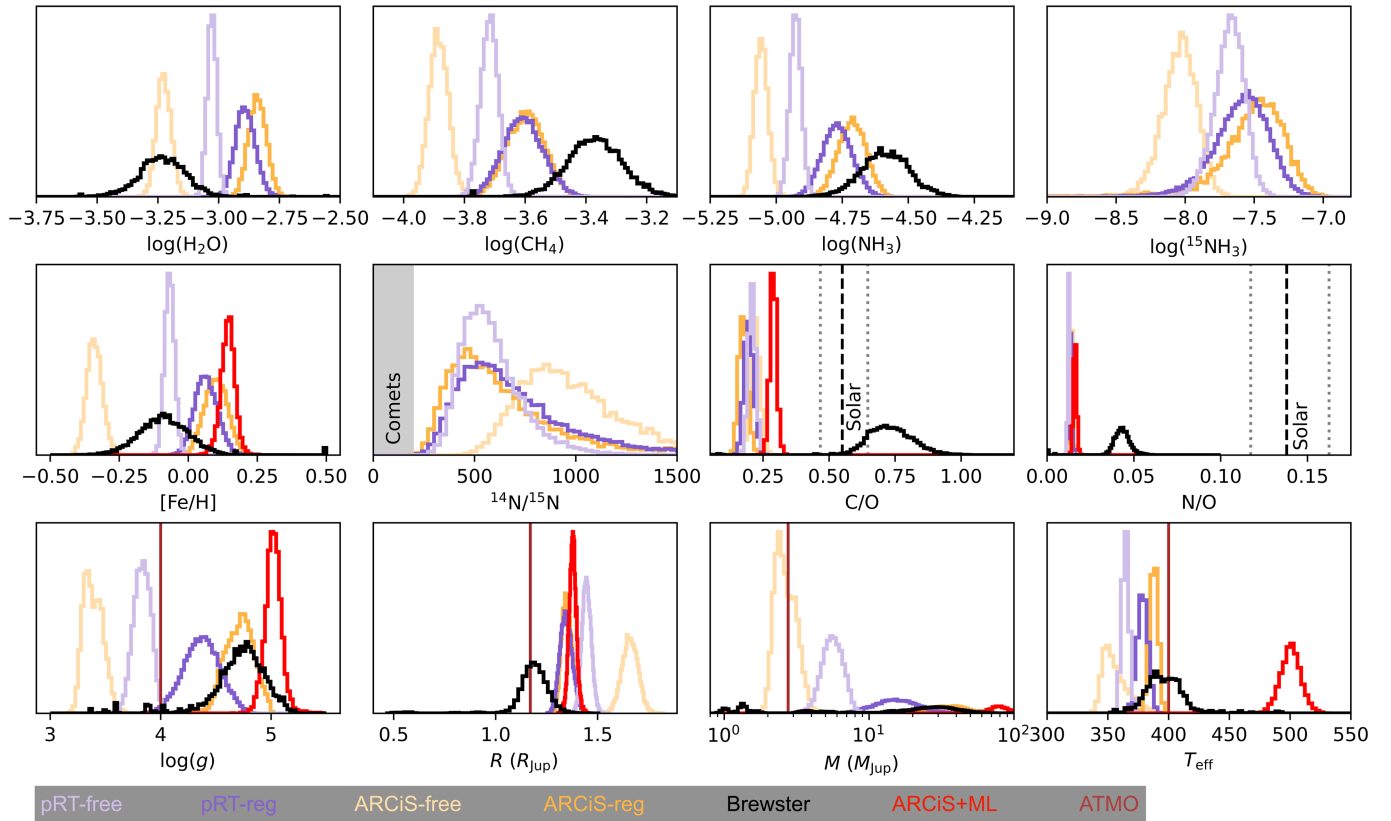
Extended Data Fig. 1 | The spectrum of WISE J1828 and the best-fit model.
 We show the MIRI/MRS spectrum of WISE J1828 (black solid lines) and the best-fit model of the regularized P - T retrieval of petitRADTRANS (red line).

Residuals (models – observed spectrum) are shown in the bottom panel. pRT-reg and ARCiS-reg stand for the regularized P - T retrieval of petitRADTRANS and ARCiS, respectively.



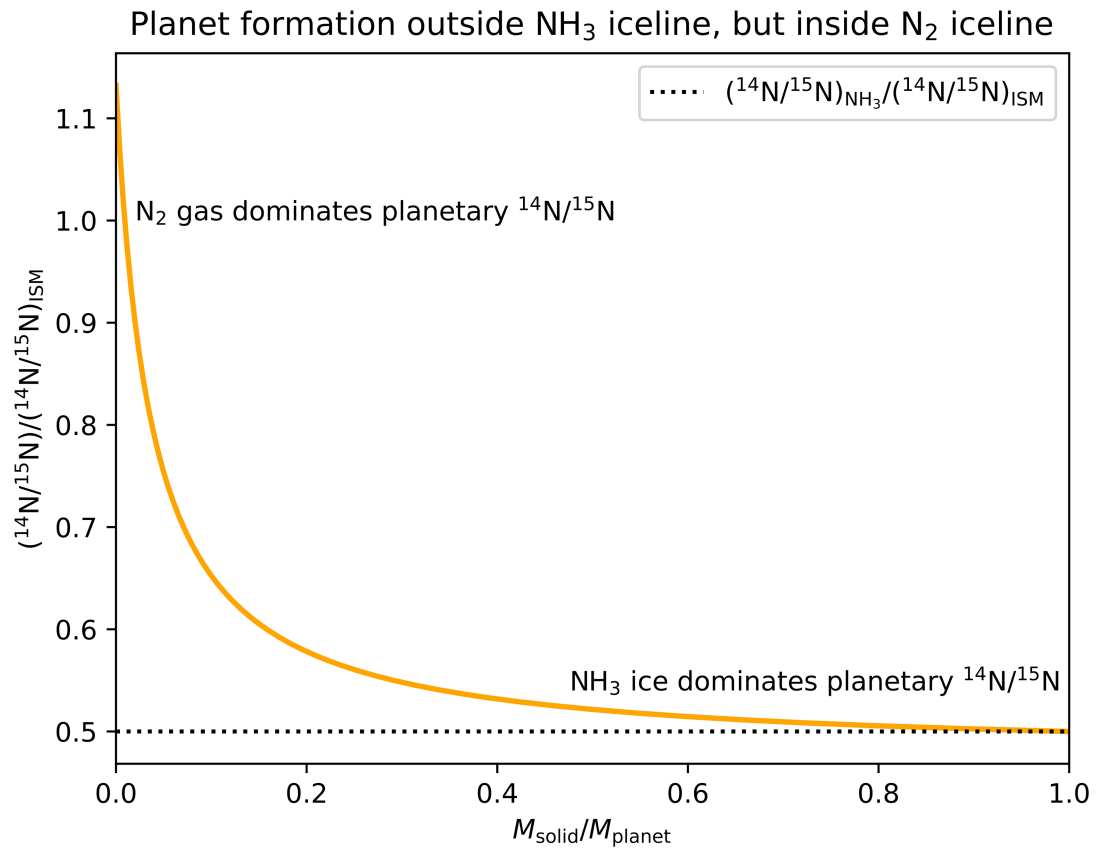
Extended Data Fig. 2 | Model inferences on the various P - T profiles derived for WISE J1828. The individual panels always highlight the constraint from one given model, whereas the results of the other models are shown in the background. pRT-reg and ARCiS-reg stand for the regularized P - T retrievals, whereas pRT-free and ARCiS-free stand for the unregularized P - T retrievals of petitRADTRANS and ARCiS, respectively. The contribution functions of the

HST and MIRI observations, constrained from the best-fit pRT-reg model, are shown as dotted and dashed lines, respectively. The condensation curve for water (at solar metallicity) is shown as a blue dash-dotted curve, indicating that, although neglected in our models, water clouds could affect the spectrum in a modest way.



Extended Data Fig. 3 | One-dimensional projection of the posterior distributions of the WISE J1828 retrievals. Values correspond to key atmospheric quantities shown in Extended Data Table 1. pRT-reg and ARCIS-reg

stand for the regularized P - T retrievals, whereas pRT-free and ARCIS-free stand for the unregularized P - T retrievals of petitRADTRANS and ARCIS, respectively.



Extended Data Fig. 4 | Evolution of the planetary $^{14}\text{N}/^{15}\text{N}$ as a function of the mass accreted in solids (rock and ice). This computation assumes a planet that forms outside the NH_3 iceline but inside the N_2 iceline. The dotted black line denotes the value expected for pure NH_3 ice.

Extended Data Table 1 | Physical constraints on WISE J1828

Quantity	Retrieval codes					Self-consistent codes	
	pRT-free	pRT-reg	ARCiS-free	ARCiS-reg	Brewster	ARCiS+ML	ATMO
T_{eff} (K)	364^{+3}_{-3}	379^{+4}_{-4}	354^{+13}_{-7}	388^{+3}_{-4}	397^{+16}_{-14}	501^{+8}_{-8}	400
$\log(g)$	$3.83^{+0.08}_{-0.08}$	$4.37^{+0.16}_{-0.17}$	$3.38^{+0.1}_{-0.08}$	$4.72^{+0.12}_{-0.14}$	$4.74^{+0.19}_{-0.21}$	$5.02^{+0.07}_{-0.07}$	4.0
R (R_{Jup})	$1.45^{+0.02}_{-0.02}$	$1.35^{+0.03}_{-0.03}$	$1.65^{+0.04}_{-0.04}$	$1.35^{+0.03}_{-0.03}$	$1.19^{+0.06}_{-0.06}$	$1.38^{+0.02}_{-0.02}$	1.17
M (M_{Jup})	$5.76^{+1.04}_{-0.89}$	$17.27^{+6.86}_{-5.01}$	$2.69^{+0.58}_{-0.40}$	$38.57^{+10.92}_{-9.66}$	$31.50^{+14.30}_{-11.60}$	$79.99^{+12.79}_{-10.87}$	2.76
R_{bin} (R_{Jup})	$1.02^{+0.02}_{-0.02}$	$0.95^{+0.02}_{-0.02}$	$1.17^{+0.03}_{-0.03}$	$0.95^{+0.02}_{-0.02}$	$0.84^{+0.04}_{-0.04}$	$0.98^{+0.01}_{-0.01}$	0.83
M_{bin} (M_{Jup})	$2.88^{+0.52}_{-0.45}$	$8.63^{+3.43}_{-2.51}$	$1.34^{+0.29}_{-0.2}$	$19.29^{+5.46}_{-4.83}$	$15.75^{+7.15}_{-5.8}$	$39.99^{+6.4}_{-5.43}$	1.38
[M/H]	$-0.07^{+0.02}_{-0.02}$	$0.06^{+0.04}_{-0.04}$	$-0.34^{+0.03}_{-0.03}$	$0.10^{+0.04}_{-0.04}$	$-0.08^{+0.10}_{-0.09}$	$0.14^{+0.02}_{-0.03}$	solar
C/O	$0.21^{+0.01}_{-0.01}$	$0.20^{+0.02}_{-0.02}$	$0.22^{+0.02}_{-0.02}$	$0.17^{+0.02}_{-0.02}$	$0.73^{+0.08}_{-0.10}$	$0.29^{+0.01}_{-0.01}$	solar
(N/O) / (N/O) $_{\odot}$	$0.091^{+0.004}_{-0.004}$	$0.096^{+0.006}_{-0.006}$	$0.107^{+0.006}_{-0.006}$	$0.097^{+0.006}_{-0.006}$	$0.314^{+0.036}_{-0.032}$	$0.117^{+0.006}_{-0.007}$	solar
$^{14}\text{N}/^{15}\text{N}$	560^{+165}_{-115}	642^{+365}_{-192}	949^{+322}_{-208}	591^{+432}_{-190}	–	–	–
$\log(\text{H}_2\text{O})$	$-3.03^{+0.02}_{-0.02}$	$-2.89^{+0.04}_{-0.04}$	$-3.23^{+0.03}_{-0.03}$	$-2.84^{+0.04}_{-0.04}$	$-3.23^{+0.10}_{-0.10}$	chem	chem
$\log(\text{CH}_4)$	$-3.72^{+0.03}_{-0.03}$	$-3.61^{+0.07}_{-0.06}$	$-3.88^{+0.03}_{-0.03}$	$-3.60^{+0.06}_{-0.06}$	$-3.36^{+0.10}_{-0.09}$	chem	chem
$\log(\text{NH}_3)$	$-4.93^{+0.02}_{-0.02}$	$-4.77^{+0.06}_{-0.06}$	$-5.06^{+0.03}_{-0.02}$	$-4.71^{+0.05}_{-0.05}$	$-4.58^{+0.10}_{-0.10}$	chem	chem
$\log(^{15}\text{NH}_3)$	$-7.67^{+0.10}_{-0.11}$	$-7.58^{+0.17}_{-0.21}$	$-8.03^{+0.11}_{-0.13}$	$-7.49^{+0.18}_{-0.25}$	–	–	–
$\log(K_{zz})$	–	–	–	–	–	$9.01^{+0.19}_{-0.19}$	7

‘free’ in the code name means that the P - T structure was not regularized, whereas this was done for the ‘reg’ cases. R_{bin} model radii have been multiplied by $1/\sqrt{2}$, assuming that WISE J1828 is an equal-property binary. R_{bin} was used for calculating M_{bin} from the inferred gravity. The units of K_{zz} are cm^2s^{-1} . ‘chem’ means that absorber abundances have been determined from a chemical model. ‘solar’ means that the parameter was not varied and that a solar composition was assumed instead.

Article

Extended Data Table 2 | Physical constraints on WISE J1828, combining different codes

Quantity	Retrievals	Self-consistent codes
T_{eff} (K)	378^{+13}_{-18}	450 ± 101
$\log(g)$	$4.34^{+0.42}_{-0.88}$	4.5 ± 1.0
R (R_{Jup})	$1.37^{+0.26}_{-0.13}$	1.27 ± 0.21
M (M_{Jup})	$15.8^{+22.82}_{-12.64}$	41*
R_{bin} (R_{Jup})	$0.97^{+0.18}_{-0.09}$	0.90 ± 0.15
M_{bin} (M_{Jup})	$7.91^{+11.33}_{-6.34}$	21*
[M/H]	$-0.05^{+0.15}_{-0.27}$	no comb
C/O	$0.21^{+0.45}_{-0.03}$	no comb
(N/O) / (N/O) _⊙	$0.10^{+0.19}_{-0.01}$	no comb
$^{14}\text{N}/^{15}\text{N}$	673^{+393}_{-212}	–
$\log(\text{H}_2\text{O})$	$-3.03^{+0.18}_{-0.21}$	chem
$\log(\text{CH}_4)$	$-3.65^{+0.21}_{-0.21}$	chem
$\log(\text{NH}_3)$	$-4.79^{+0.15}_{-0.25}$	chem
$\log(^{15}\text{NH}_3)$	$-7.68^{+0.24}_{-0.34}$	–
$\log(K_{zz})$	–	8 ± 2

R_{bin} model radii have been multiplied by $1/\sqrt{2}$, assuming that WISE J1828 is an equal-property binary. R_{bin} was used for calculating M_{bin} from the inferred gravity. The units of K_{zz} are $\text{cm}^2 \text{s}^{-1}$. ‘chem’ means that absorber abundances have been determined from a chemical model. ‘no comb’ means that the respective parameter was only varied in one of the two codes; see Extended Data Table 1 for the inferred values. * for the inferred average mass denotes that the distance between the solutions of the two codes was larger than the average value, so no uncertainties, derived as explained in the Methods section, are given here.